ACS Catalysis
pubs.acs.org/acscatalysis
Research Article

# Effect of Support on Oxygen Reduction Reaction Activity of Supported Iron Porphyrins

Qi Hua, Kenneth E. Madsen, Anne Marie Esposito, Xinyi Chen, Toby J. Woods, Richard T. Haasch, Shuting Xiang, Anatoly I. Frenkel, Timothy T. Fister, and Andrew A. Gewirth*

Cite This: ACS Catal. 2022, 12, 1139−1149
Read Online



**ABSTRACT:** We report the oxygen reduction reaction (ORR) activity in acid of an Fe porphyrin on different supports. While the activity is high ($E_{1/2}$ = 0.34 V vs RHE with $n$ = 3.8) when the Fe porphyrin is adsorbed on XC72 (a graphitic carbon), this activity is much lower when the porphyrin is adsorbed on either $MoS_2$ ($E_{1/2}$ = −0.15 V vs RHE with $n$ = 2.2) or g-$C_3N_4$ ($E_{1/2}$ = −0.24 V vs RHE with $n$ = 3.1). Electron paramagnetic resonance (EPR), X-ray absorption fine structure (XAFS), and magnetometry measurements show the electronic structure around the Fe center is the same for all three supports. Only the Fe porphyrin supported on XC72 exhibits a pH dependence in its ORR activity. This observation, coupled with the increased hydrophilicity of XC72 relative to the other supports, suggests that the support-electrolyte interaction controls the ORR activity. Modification of $MoS_2$ to increase its hydrophilicity results in a more active ORR catalyst.

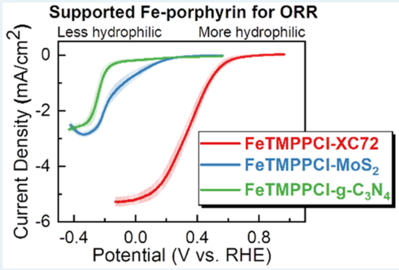


**KEYWORDS:** *oxygen reduction reaction, iron porphyrin, carbon, $MoS_2$, carbon nitride, hydrophilicity*



## 1. INTRODUCTION

Proton exchange membrane fuel cells (PEMFCs) and rechargeable metal-air batteries (MABs) are next-generation energy devices for clean power generation.[1,2] The kinetics of the oxygen reduction reaction (ORR) at the cathode in PEMFCs or MABs is slow relative to hydrogen oxidation occurring at the anode, and consequently, substantial effort attends the search for effective ORR electrocatalysts.[3,4] The most commonly used electrocatalysts for the ORR are based on Pt or Pt-alloys, materials which have shortcomings associated with low abundance, high price, and degradation (or poisoning) during the ORR operation.[5] Nonprecious metal (NPM) catalysts are earth-abundant alternatives to Pt-based catalysts with lower price and comparable activity, at least in alkaline electrolytes.[3,6−8] Recent years have witnessed significant improvements regarding the activity and durability of NPM catalysts, but the systematic development of these materials is hampered by uncertainty regarding the nature of the active sites and the ORR mechanism.[1,9] The requirement of high temperature pyrolysis for better ORR performance of NPM catalysts implies that the structures of the catalyst precursors are significantly altered, leading to heterogeneity in Fe speciation in the catalyst with the probable inclusion of $FeN_4$,[10,11] $Fe_xN$,[12] $Fe_3C$,[13] and Fe(0).[14,15] This heterogeneity complicates both characterization and developing correlations between active site structure and reactivity.[2]

One way to circumvent the Fe characterization issue is to use nonpyrolyzed macrocycle complexes (such as Fe porphyrins or Fe phthalocyanines), where the well-defined structure is preserved during catalyst synthesis. This structural preservation in concept allows direct correlation between the catalyst structure and the resulting ORR activity.[1,16] Indeed, the first NPM catalysts used intact metalated porphyrins or phthalocyanines adsorbed on carbon surfaces.[10,17] The observation that pyrolysis yields a more active ORR material directed much subsequent activity away from the use of intact porphyrins or phthalocyanines. Nonetheless, numerous studies on nonpyrolyzed macrocycle complexes as ORR catalysts have characterized the molecular structure after their absorbing or coordinating on supports.[16,18] For example, studies have addressed molecular materials adsorbed on carbon nanotubes,[9,19] multiwall carbon nanotubes,[20] reduced graphene oxide (rGO),[21] a graphene-metal oxide framework composite,[22] and a covalent oxide framework.[23] These analyses suggested that the molecular material remained intact following adsorption on carbon supports, with a relatively weak interaction between the support and the macrocycle.

Relatively little work addresses adsorption of Fe-containing macrocycles on noncarbon supports for ORR purposes. Co or Fe macrocycles adsorbed onto Au electrodes modified with self-assembled monolayers (SAMs) demonstrate ORR activity, albeit at somewhat higher overpotentials.[24−32]

Received: October 22, 2021
Revised: December 7, 2021




https://doi.org/10.1021/acscatal.1c04871
ACS Catal. 2022, 12, 1139−1149

Kwon et al. reported that a two-dimensional $MoS_2$/Fe-phthalocyanine (FePc) hybrid exhibited an ORR $E_{1/2} \sim 0.89$ V in alkaline solution.[33] The $MoS_2$ hybrid reported by these authors was synthesized by using a hydrothermal method at 200 °C, and this method led to a metastable metallic 1T′ phase of $MoS_2$ rather than the semiconducting 2H phase found in commercial $MoS_2$. In addition, this method results in a nonplanar geometry of the Fe−$N_4$ active site of FePc, which the authors associated with the high ORR catalytic activity of the $MoS_2$ hybrid.

Mesoporous carbon nitride (MCN) has been evaluated as a support for both metal (Mn, Fe, Co, Ni, Cu, and Zn) phthalocyanine and Co porphyrin ORR catalysts by Singh et al.[34,35] The MCN was synthesized by a hard templating method to improve the surface area and conductivity of the support. The highest $E_{1/2}$ (~0.05 V) is exhibited by CoPc@MCN in these reports, with a limiting current density < 1.5 mA/cm$^2$ and $n \sim 1.64$ in 0.1 M $HClO_4$ with rotation. This activity is much lower than that found using carbon-based supports.

In this paper, we use a ball-milling method to synthesize nonpyrolyzed Fe porphyrin absorbed on three different supports, i.e., XC72, 2H-$MoS_2$, and g-$C_3N_4$, as ORR catalysts. We find that while the electronic structure around the Fe center is identical as demonstrated by several physical characterization techniques, the ORR activity of three catalysts shows significant variance. The origin of this variance is found to be associated with differences in the support-electrolyte interaction among the different materials. A modification to $MoS_2$ to improve its hydrophilicity leads to enhanced ORR activity, a result which further corroborates the importance of support-electrolyte interactions in Fe-based ORR activity. Although the ORR activity exhibited by our catalysts is low relative to other materials, particularly those processed using pyrolysis, this work provides insight into the effect of the support and particularly its interaction with the electrolyte on ORR performance from a fundamental perspective.

## 2. EXPERIMENTAL SECTION

**2.1. Catalyst Preparation.** *Preparation of Catalyst on Support.* 5,10,15,20-Tetrakis(4-methoxyphenyl)-21H,23H-porphine iron(III) chloride (FeTMPPCl) was purchased from Frontier Scientific and used without further purification. The three support materials used were Vulcan XC72 (Fuel Cell Store, College Station, TX), $MoS_2$ (Sigma-Aldrich, St. Louis, MO), and carbon nitride (g-$C_3N_4$). In a typical experiment, 300 mg of Fe porphyrin and 900 mg of support material were placed into a 50 mL agate ball-milling container with 12 g agate balls. The container was then fixed into the planetary ball-mill (Mini-Planetary Mill Model PMV1-0.4L, MSE Supplies LLC) and agitated at 400 rpm for 50 min. The resulting catalyst powder was used as prepared. Samples are delineated by name and support (i.e., FeTMPPCl-XC72 is FeTMPPCl supported on XC72).

Catalysts were also prepared by using a wet impregnation method following prior reports.[36] Here, 300 mg of Fe porphyrin was placed into a beaker containing 30 mL of $(CH_3)_2CO$ and 900 mg of support. The suspension was stirred for 2 h. Then, the solvent was completely evaporated, first with the help of a heating plate and finally in an oven at 75 °C overnight. Catalysts prepared using this wet impregnation method gave ORR responses identical with those prepared using the dry method above. The dry method was chosen to simplify preparation of multiple materials.

*Preparation of Graphitic Carbon Nitride g-$C_3N_4$.* Carbon nitride g-$C_3N_4$ was prepared by following a published method.[37] In a typical synthesis, 10 g of urea powder was placed into an alumina crucible, covered with aluminum foil, and then heated at a ramp rate of 15 °C/min to a final temperature of 550 °C. The sample was maintained at this temperature for 2 h before being allowed to cool to room temperature at a rate of 90 °C/min, yielding a pale-yellow powder. XRD yielded diffraction peaks identical with those expected for g-$C_3N_4$.[38]

*Synthesis of the $MoS_2$-200 and $MoS_2$-220.* The oxygen-incorporated $MoS_2$ ($MoS_2$-200) was prepared by following a published method.[39] Typically, 1 mmol of $(NH_4)_6Mo_7O_{24}\cdot 4H_2O$ and 30 mmol of thiourea were dissolved in 35 mL of distilled water under vigorous stirring to form a homogeneous solution. After being stirred for 30 min, the solution was transferred into a 45 mL Teflon-lined stainless steel autoclave, sealed, and maintained at 200 °C for 24 h. Then, the reaction system was allowed to cool down to room temperature. The black product, $MoS_2$-200, was collected by centrifugation, washed with distilled water and ethanol, and dried at 60 °C under vacuum. As a control, $MoS_2$-220 with diminished oxygen incorporation[40,41] was synthesized using the same method except the autoclave temperature was 220 °C. XRD obtained from these materials was consistent with the literature.[39]

**2.2. Electrochemical Experiments.** All electrochemical measurements were performed in a three-compartment electrochemical cell. The counter electrode was a carbon rod, and the reference electrode was a “leakless” Ag/AgCl reference electrode (3 M KCl, eDAQ, Inc.). The glassy carbon disk ($A$ = 0.283 cm$^2$), which served as the working electrode, was polished sequentially with 0.25 and 0.05 $\mu$m diamond polish (Buehler) and sonicated in water before use. Aqueous electrolyte solutions were prepared using Milli-Q purified water (>18 MΩ cm) and the corresponding salts. Solutions were sparged with $O_2$ or Ar prior to each measurement for 30 min.

Catalyst inks were prepared by combining 5 mg of catalyst, 175 $\mu$L of ethanol, and 47.5 $\mu$L of Nafion (Sigma-Aldrich) in a planetary mixer (Thinky). After mixing, 5 $\mu$L of catalyst ink was drop-cast onto the glassy carbon electrode. Linear sweep voltammetry (LSV) was measured with a rotating disk electrode (RDE) using a 760D Electrochemical Workstation (CH Instruments, Austin, TX) and a MSRX rotator (Pine Instruments, Durham, NC) between relevant voltages, with a 0.01 V/s scan rate in $O_2$-saturated 0.1 M $HClO_4$ or buffer solutions at a rotation rate of 1600 rpm. All potentials were converted to a reversible hydrogen electrode (RHE) by measuring the open-circuit potential of a flame-annealed Pt wire electrode in a $H_2$ gas-saturated electrolyte immediately following measurements. Values reported reflect the results of at least three independent measurements.

Buffer solutions for pH 2−6 were prepared by Briton-Robinson buffers[42] consisting of mixtures of 0.04 M $H_3BO_3$ (EM SCIENCE), 0.04 M $H_3PO_4$ (Sigma-Aldrich) and 0.04 M $CH_3COOH$ (Fisher Scientific) titrated to the desired pH with 0.2 M NaOH (Sigma-Aldrich). A solution of 0.1 M $HClO_4$ acid (Sigma-Aldrich) was used for pH 1 electrolyte. The pH values were measured using an Orion Star A111 pH meter (Thermo Scientific).


https://doi.org/10.1021/acscatal.1c04871
ACS Catal. 2022, 12, 1139−1149

**2.3. Physical Characterization.** ICP-OES was carried out on a PerkinElmer 2000 DV in the University of Illinois SCS Microanalysis Laboratory. XPS was performed using a Kratos AXIS Ultra spectrometer with a monochromatic Al K$\alpha$ (1486.6 eV) X-ray source. All binding energies were referenced to graphitic carbon at 284.5 eV. Superconducting quantum interference device (SQUID) magnetometry was collected at 300 K (27 °C) by using a Magnetic Property Measurement System (Quantum Design). The sample was placed in a polycarbonate capsule, secured with Kapton tape, and inserted into a plastic straw. Powder X-ray diffraction was performed using a Siemens/Bruker D5000 diffractometer with Cu K-$\alpha$ radiation ($\lambda$ = 0.15418 nm). X-band electron paramagnetic resonance (EPR) spectra were recorded using a Bruker 10″ EMXPlus X-band CW spectrometer at 10 K for ethanoic suspensions of materials containing 200 $\mu$mol/L Fe. Q-band EPR spectra were recorded for catalyst power in solid state at 10 K on a Bruker Elexsys E-580 Q-band CW spectrometer. Fits to the EPR spectra were obtained by using the EasySpin program.[43] X-ray absorption spectroscopy was carried out at beamline sector 9-BM at the Advanced Photon Source at Argonne National Laboratory with a beam cross section of 2.6 × 0.75 mm$^2$. Samples were studied *ex situ* by pressing the catalyst powder into a pellet. Fe K-edge absorption data for materials supported on XC72 and g-$C_3N_4$ were recorded in transmission mode. Measurements for materials supported on $MoS_2$ were recorded in fluorescence mode. All measurements used a double-crystal Si (111) monochromator run at 50% detuning and ion chamber detectors filled with a mixture of He/$N_2$. X-ray absorption near edge structure (XANES) and extended X-ray absorption fine structure (EXAFS) data were processed and analyzed with Athena and Artemis programs of the Demeter data analysis package[44] that utilizes the FEFF6 program[45] to fit the EXAFS data.

Contact angle measurements were carried out using a Ramé-Hart contact angle goniometer (model 250). Samples were first pressed into solid pellets (2500 PSI, 5 min) to yield sufficiently smooth and flat surfaces for analysis. Each measurement was conducted by placing 1 $\mu$L of deionized water onto the surface of the pellet using a microsyringe. Contact angles were then computed from an average of 20 tangent line measurements between the substrate and the drop.

## 3. RESULTS

**3.1. ORR Activity.** Figure 1 presents linear sweep voltammograms obtained from a RDE rotating at 1600 rpm coated with FeTMPPCl adsorbed on different supports in $O_2$-saturated 0.1 M $HClO_4$. The Ar control is shown as the gray line in the figure. The red line in Figure 1 shows that FeTMPPCl-XC72 exhibits an $E_{1/2}$ of 0.34 ± 0.02 V vs RHE. Koutecký-Levich (K-L) measurements (Figure S1a,d) show that the reduction consumes $n$ = 3.8 ± 0.1 $e^-$ with a calculated production of 11 ± 5% $H_2O_2$. Both $E_{1/2}$ and $n$ values are consistent with prior reports.[9,46−48]

The blue line in Figure 1 shows that FeTMPPCl-$MoS_2$ exhibits an $E_{1/2}$ of −0.15 ± 0.03 V vs RHE. K-L measurements (Figure S1b,e) show that the reduction consumes $n$ = 2.24 ± 0.02 $e^-$ with a calculated production of 88 ± 1% $H_2O_2$. The green line in Figure 1 shows that FeTMPPCl-g-$C_3N_4$ exhibits an $E_{1/2}$ of −0.23 ± 0.02 V vs RHE. K-L measurements (Figure S1c,f) show that the reduction consumes $n$ = 3.13 ± 0.04 $e^-$ with 44 ± 2% $H_2O_2$ produced. Interestingly, the FeTMPPCl on XC72 is substantially more active for the ORR both in terms of $E_{1/2}$ and $n$ values relative to FeTMPPCl on either of the other supports.

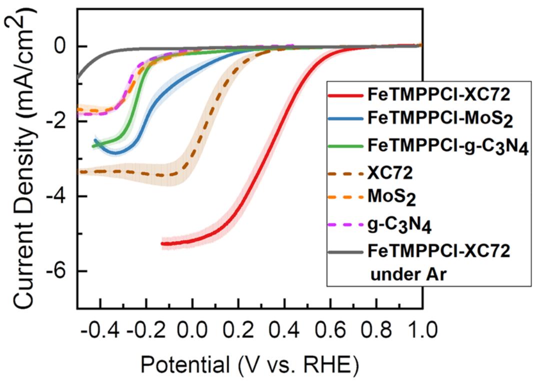


**Figure 1.** Ar-subtracted LSV obtained from FeTMPPCl-XC72, FeTMPPCl-$MoS_2$, FeTMPPCl-g-$C_3N_4$, XC72, $MoS_2$, and g-$C_3N_4$ in $O_2$-saturated 0.1 M $HClO_4$ using a RDE at 1600 rpm. The shaded areas represent ± 1 SD in the current obtained from multiple measurements. The gray line was obtained from FeTMPPCl-XC72 in 0.1 M $HClO_4$ absent $O_2$.

Figure 1 also shows the results of ORR measurements obtained from the supports absent FeTMPPCl. While FeTMPPCl-XC72 exhibits a ca. 258 mV shift in $E_{1/2}$ relative to bare XC72, the FeTMPPCl-$MoS_2$ and FeTMPPCl-g-$C_3N_4$ exhibit a ca. 99 mV and 31 mV shift in $E_{1/2}$ relative to bare $MoS_2$ and bare g-$C_3N_4$, respectively. Thus, the results in Figure 1 show that ORR activity varies as FeTMPPCl-XC72 > FeTMPPCl-$MoS_2$ > FeTMPPCl-g-$C_3N_4$. The ORR activity of bare $MoS_2$[49,50] and bare g-$C_3N_4$[51] is consistent with prior results. The XC72 supported porphyrin is substantially more active relative to the same material supported on $MoS_2$ or g-$C_3N_4$. Figure S2 shows the results for the supports obtained absent $O_2$ and indicates the current in Figure 1 is associated with the ORR. Figure S3 shows ORR activity obtained for the three systems considered here in 0.1 M KOH. While FeTMPPCl-XC72 exhibits good activity, the ORR activity from FeTMPPCl-$MoS_2$ and FeTMPPCl-g-$C_3N_4$ is again diminished relative to the XC72 support and is convolved with the response obtained from bare glassy carbon.

**3.2. ICP and Electrochemical Results.** ICP-OES results (Table S1) obtained prior to immersion show that the amount of Fe on the electrode surface is nearly the same for the three materials. In order to evaluate the presence of leaching during the ORR measurement, ICP-OES was performed on the electrolyte solution following ORR. These measurements (Table S1) show no evidence for Fe, suggesting that the electrode supports do not leach Fe during the ORR measurement. Consequently, the origin of the diminished activity for both FeTMPPCl-$MoS_2$ and FeTMPPCl-g-$C_3N_4$ relative to FeTMPPCl-XC72 is not loss of Fe into the electrolyte solution.

Another possible origin of differences between the different supports is their bulk conductivity. Indeed, the bulk conductivity of quasimetallic XC72 (2.77 S·cm$^{-1}$)[52] is greater than that found for semiconducting 2H-$MoS_2$ (1.3 × 10$^{-5}$ S·cm$^{-1}$)[53] or semiconducting g-$C_3N_4$ (∼10$^{-12}$ S·cm$^{-1}$).[54] In concept, this difference in bulk conductivity could be the origin of the lower ORR activity seen in FeTMPPCl supported on $MoS_2$ or g-$C_3N_4$. Indeed heterogeneous rate constants for the $[Fe(CN)_6]^{3-/4-}$ couple on graphite (pristine basal plane: 6.8 × 10$^{-4}$ cm·s$^{-1}$; defective basal plane: 5.9 × 10$^{-4}$ cm·s$^{-1}$)[55] are 5−


https://doi.org/10.1021/acscatal.1c04871
ACS Catal. 2022, 12, 1139−1149

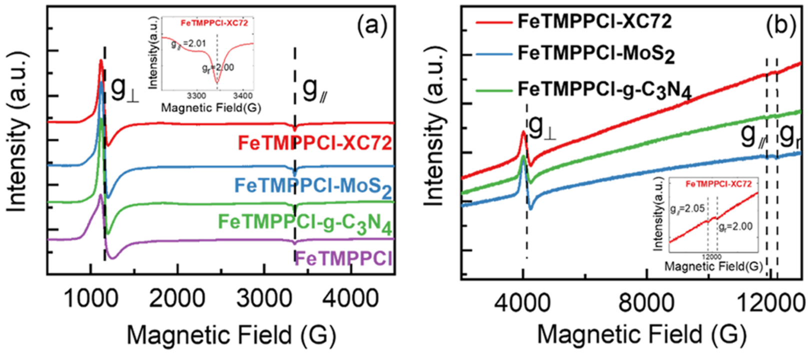


**Figure 2.** EPR of FeTMPPCl-XC72, FeTMPPCl-$MoS_2$, and FeTMPPCl-g-$C_3N_4$ obtained at 10 K: (a) X-band along with unsupported FeTMPPCl. The dashed lines demarcate $g$ = 5.88, 2.01, and 2.00 (l−r). Inset: enlargement of the 3220−3420 G field region of FeTMPPCl-XC72; (b) Q-band (solid state). The dashed lines demarcate $g$ = 5.99, 2.05, and 2.00 (l−r). Inset: enlargement of the 100350−13790 G field region of FeTMPPCl-XC72.

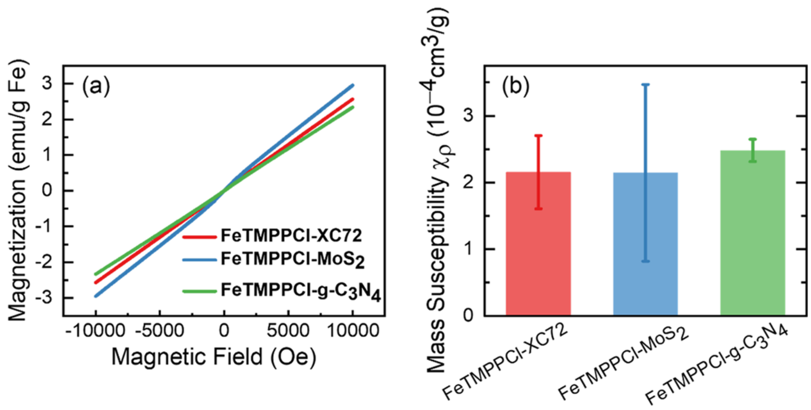


**Figure 3.** (a) SQUID magnetometry and (b) susceptibility of FeTMPPCl-XC72, FeTMPPCl-$MoS_2$, and FeTMPPCl-g-$C_3N_4$ at 300 K (27 °C). Error bars represent the SD obtained from multiple measurements.

30-fold larger than those found on $MoS_2$ (pristine basal plane: $2.1 \times 10^{-5}$ cm·s$^{-1}$; defective basal plane: $1.2 \times 10^{-4}$ cm·s$^{-1}$).[55]

In order to compare the heterogeneous rate constants for the $[Fe(CN)_6]^{3-/4-}$ couple with those for ORR, we obtained (Figure S4a) the heterogeneous rate constant $k_f$ for ORR at 0.34 V vs RHE (the $E_{1/2}$) from FeTMPPCl-XC72. This value ($1.1 \times 10^{-2}$ cm·s$^{-1}$) is substantially greater than that estimated at this potential for either FeTMPPCl-$MoS_2$ ($2.2 \times 10^{-4}$ cm·s$^{-1}$) (Figure S4b) or FeTMPPCl-g-$C_3N_4$ ($1.8 \times 10^{-4}$ cm·s$^{-1}$) (Figure S4c). In this case, supporting FeTMPPCl on either $MoS_2$ or g-$C_3N_4$ leads to rate constants at least 50 times smaller at 0.34 V relative to that found from FeTMPPCl-XC72. Since the drop in rate for ORR is much greater than that found for the $[Fe(CN)_6]^{3-/4-}$ couple, we suggest there must be an addition origin of the drop in ORR rate for FeTMPPCl supported on $MoS_2$ or g-$C_3N_4$ relative to XC72.

**3.3. Electronic Structure Characterization.** In order to evaluate possible electronic structural changes to the FeTMPPCl when combined with different supports, we obtained EPR, EXAFS, and susceptibility measurements on the different systems.

*3.3.1. EPR.* X-band EPR of FeTMPPCl-XC72 (Figure 2a) shows the presence of bands at $g_\perp$ = 5.88 and $g_\parallel$ = 2.01 as expected for a square-pyramidal ferric high-spin $FeN_4$ site with Cl as the axial ligand. These EPR values are consistent with those previously observed for 5-fold-coordinated ferric high-spin porphyrins ($g_\perp$ = 6 and $g_\parallel$ = 2) and originate from the |5/2; ±1/2> ground-state Kramers doublet of an $S$ = 5/2 spin system in an axial ligand field with positive $D$ and a rhombicity parameter $E/D \approx 0$.[56]

Figure 2a shows that all three supported samples exhibit the same signal positions and shapes as found for FeTMPPCl alone. Table S2 reports the results of fits to these EPR spectra yielding $g$ values and line widths nearly identical for the three supported samples. This result suggests that the Fe environment on each of the supported samples is identical and suggests as well that the Fe coordination environment does not change following deposition on the support. The broadened $g$ = 5.88 peak for FeTMPPCl alone likely results from an interaction between FeTMPPCl and ethanol in the suspension (the OH group weakly coordinates at the sixth axial position of the iron porphyrin), while for supported FeTMPPCl, the sixth axial position is more likely to interact with the support and less with ethanol.

Figure 2b shows the results of 10 K Q-band EPR obtained from the solid samples without ethanol addition. The higher resolution Q-band measurement resolves the presence of two features around $g$ = 2. For better clarification, the inset of Figure 2a and Figure 2b shows an enlargement of the $g$ = 2 field region obtained from FeTMPPCl-XC72 with X-band and Q-band EPR, respectively. In X-band EPR, the $g$ = 2 signal contains two unresolved features. In the Q-band EPR, the $g$ = 2 signal is resolved as $g$ = 2.05 and $g_r$ = 2.00. The $g_\parallel$ = 2.05 is associated with the axial coordination of the Fe porphyrin. The $g_r$ = 2.00 band originates from delocalized radicals in the substrate, as EPR obtained from the substrates alone also


https://doi.org/10.1021/acscatal.1c04871
ACS Catal. 2022, 12, 1139−1149

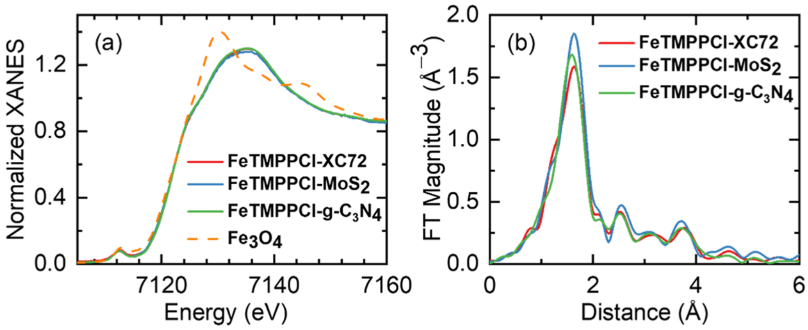


**Figure 4.** Fe K-edge X-ray absorption spectra for FeTMPPCl-XC72, FeTMPPCl-$MoS_2$, and FeTMPPCl-g-$C_3N_4$. (a) XANES and (b) Fourier transform magnitudes of the $k^2$-weighted EXAFS spectra. $Fe_3O_4$ reference spectrum is shown by a dashed line in (a).

exhibits the $g_r = 2$ feature (XC72: $g$ = 2.003−2.005;[57,58] $MoS_2$: $g$ = 2.005;[59,60] g-$C_3N_4$: $g$ = 2.003[61,62]). Again, the identical $g$ values between FeTMPPCl on the different supports suggest the presence of identical Fe environments.

*3.3.2. Magnetometry.* Figure 3a shows the change in magnetization with applied field of each material normalized to the total Fe percentage (Table S1) at 300 K. All samples exhibit linear responses suggesting that the iron porphyrin molecules are well-dispersed in the supports and that the entire material is paramagnetic. Figure 3b shows the calculated mass susceptibility along with error bars obtained from multiple measurements for the three supported materials. All materials exhibit mass susceptibilities $\chi_\rho$ = 2−2.5 × $10^{-4}$ $cm^3/g$ and result in effective magnetic moment $\mu_{eff}$ = 5.5−5.9 $\mu_B$, which is consistent with the presence of high-spin $Fe^{3+}$ (5.92 $\mu_B$).[63] The similar values between the different materials suggest that there is no superparamagnetic or ferromagnetic material in all the samples.

*3.3.3. XANES and EXAFS.* In order to obtain further insight into the electronic structure around the Fe center in the supported FeTMPPCl materials, we collected *ex situ* XANES and EXAFS data for all three samples. Figure 4a shows the Fe K-edge XANES obtained from FeTMPPCl-XC72, FeTMPPCl-$MoS_2$, and FeTMPPCl-g-$C_3N_4$. Figure 4a shows that the XANES spectra for all three materials are nearly identical in both peak shape and peak position. All three samples exhibit an edge energy of 7124 eV as has been seen previously for FeTMPPCl alone.[64−67]

Figure 4a also shows that all three samples exhibit similar 1s → 3d pre-edge features at 7113 eV. This region in energy is often used to detect, qualitatively, whether the Fe sites exhibit deviation from central symmetry, as they do in the case of $Fe_3O_4$ that contains some Fe sites in tetrahedral positions. In the case of the three samples studied here, the presence of the pre-edge feature at the 7113 eV is consistent with the square pyramidal ($C_{4v}$) symmetry.[64,67]

Figure 4b shows the Fe K-edge EXAFS data. The best fits of theoretical EXAFS spectra to experimental data are shown in Figure S5. Table 1 reports the quantitative fitting results. We note that the amplitude factor and coordination numbers correlate in the EXAFS equation; and for quantitative analysis of the data, it is common to assume that the amplitude factor in the unknown sample is the same as in a reference sample, and the coordination numbers in the unknown sample are varied in the fits. In this case, due to the lack of an appropriate experimental reference with a similar local environment as in the unknown samples, we examined two possibilities for choosing the better model for analysis. First, when the total coordination number was fixed as 5 (4N+1Cl), the amplitude factor was found to be 1.4, i.e., unphysically large.[68,69] On the other hand, a coordination number of 6 (4N+1Cl+1O) gave a physically reasonable amplitude factor of 1.0. We note that XPS data obtained from FeTMPPCl on different supports exhibits an O signal, contributing ca. 5%−10% to the total signal after accounting for sensitivity factors (Figure S6). That observation is an independent factor in favor of the second model, with CN = 6. The contribution of O was modeled by using an additional Fe−N bond, a well-justified approach because the backscattering amplitude of Fe−N and Fe−O paths is very similar.

**Table 1. Best Fit Structural Parameters Obtained from the Analysis of EXAFS Data[a]**

| samples | contribution | CN | $R$ (Å) | $\sigma^2$ (Å$^2$) |
|---|---|---|---|---|
| FeTMPPCl-XC72 | Fe−Cl | 1 | 2.28(2) | 0.003(2) |
| | Fe−N(O) | 5 | 2.06(1) | 0.007(2) |
| FeTMPPCl-$MoS_2$ | Fe−Cl | 1 | 2.28(4) | 0.002(4) |
| | Fe−N(O) | 5 | 2.05(2) | 0.004(3) |
| FeTMPPCl-g-$C_3N_4$ | Fe−Cl | 1 | 2.30(2) | 0.004(2) |
| | Fe−N(O) | 5 | 2.05(1) | 0.006(2) |

[a]Interatomic distances $R$ with uncertainties in parentheses, bond length disorder factors $\sigma^2$, and coordination numbers (CN) for the nearest coordination shells for FeTMPPCl-XC72, FeTMPPCl-$MoS_2$, and FeTMPPCl-g-$C_3N_4$.

Interestingly, XPS obtained from FeTMPPCl on all three supports exhibited Fe-related peaks at nearly identical energies (Figure S7, Table S3). Uncertainties in the last significant digit are given in parentheses.

Table 1 shows the Fe−N and Fe−Cl bond lengths from FeTMPPCl are nearly independent of the support. Additionally, the Fe−N and Fe−Cl bond lengths are also very close to those in the FeTMPPCl unsupported crystal structure[70] ( Fe−$N_{ave}$ = 2.064 Å, Fe−Cl = 2.240 Å). This close correspondence suggests there is only a weak interaction between the iron porphyrin and the different supports.

*3.3.4. pH Dependent Measurements.* We next examine the effect of changing solution pH on the ORR activity of the supported porphyrins. Figure 5 shows that the ORR activity of FeTMPPCl-XC72 changes as a function of solution pH. Alternatively, changing the pH for either FeTMPPCl-$MoS_2$ or FeTMPPCl-g-$C_3N_4$ results in little change in ORR activity. Thus, the XC72 support imparts a pH dependence which is not observed on either $MoS_2$ or g-$C_3N_4$.

Figure 6a plots the pH dependence of $E_{1/2}$ values obtained from ORR of FeTMPPCl on the different supports. On XC72, the $E_{1/2}$ first decreases from 0.31 V at pH 1 to 0.10 V at pH 3


https://doi.org/10.1021/acscatal.1c04871
ACS Catal. 2022, 12, 1139−1149

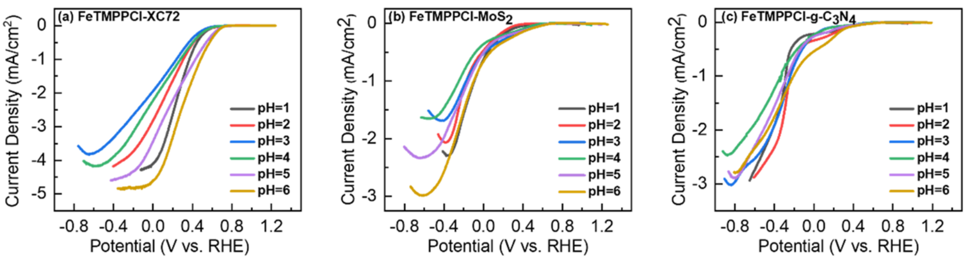


**Figure 5.** LSV of (a) FeTMPPCl-XC72, (b) FeTMPPCl-$MoS_2$, and (c) FeTMPPCl-g-$C_3N_4$ at $O_2$-saturated different pH solutions obtained at a rotation rate of 1600 rpm.

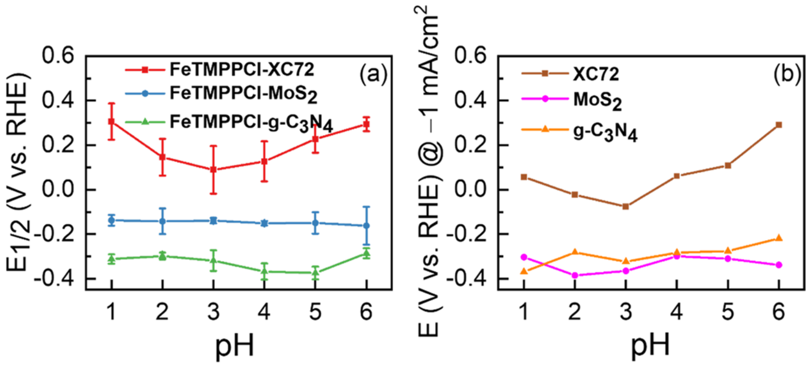


**Figure 6.** pH dependence of (a) $E_{1/2}$ values from LSV of FeTMPPCl-XC72, FeTMPPCl-$MoS_2$, and FeTMPPCl-g-$C_3N_4$ and (b) the ORR potential obtained at an ORR current density of −1 mA/cm$^2$ from LSV of bare XC72, $MoS_2$, and g-$C_3N_4$.

($n$ = 3.21) and then increases to 0.30 V at pH 6 ($n$ = 3.99). The variation in $E_{1/2}$ is over 200 mV between the different pH values examined. Indeed, a pH-dependent onset for ORR has also been observed in pyrolyzed NPM materials.[71] Figure 6a also shows the pH dependence of the $E_{1/2}$ values for both FeTMPPCl-$MoS_2$ and FeTMPPCl-g-$C_3N_4$. In contrast to the XC72 case, the $E_{1/2}$ values from FeTMPPCl on either $MoS_2$ or g-$C_3N_4$ change by between 20 and 80 mV over the pH range examined. Figure 6b reports differences in the ORR onset (defined as −1 mA/cm$^2$ reduction current density; we used the onset potential because the limiting current was not achieved for these bare supports) for the different supports without adsorbed FeTMPPCl. Consistent with the results in Figure 6a, XC72 exhibits pH dependence, with higher onset potentials at pH 1 and 6 and a minimum between pH 3 and 4. Alternatively, neither bare $MoS_2$ or bare g-$C_3N_4$ exhibit substantial pH dependence in the ORR onset potential.

The variation in pH dependence with the different supports suggests that the interaction with the solution is different among the three supports examined. Indeed, contact angle measurements suggest that XC72 is somewhat more hydrophilic (contact angle = 43°[72]) relative to either $MoS_2$ (contact angle = 83°[73]) or g-$C_3N_4$ (contact angle = 74°[74]). In turn, this observation suggests that the ORR onset and $n$ value, both for bare and FeTMPPCl-supported systems, depends on the interaction of the support with water.

*3.4.5. ORR of FeTMPPCl on Activated $MoS_2$.* In order to test whether substrate wettability affects ORR parameters, we synthesized two additional supports based on $MoS_2$. By using a hydrothermal synthetic method at different processing temperatures, different amounts of O can be incorporated into $MoS_2$.[39] Processing at 200 °C yields O-incorporated $MoS_2$-200[39,75] while processing at 220 °C yields a defect-rich $MoS_2$.[40] The incorporation of O leads to an increased $c$-axis spacing in $MoS_2$-200 (9.5 Å) relative to either commercial $MoS_2$ or $MoS_2$-220 (6.15 Å).[39,75]

Figure 7a shows Ar-subtracted LSV obtained from FeTMPPCl-$MoS_2$-200, $MoS_2$-200, $MoS_2$-220, and $MoS_2$ in

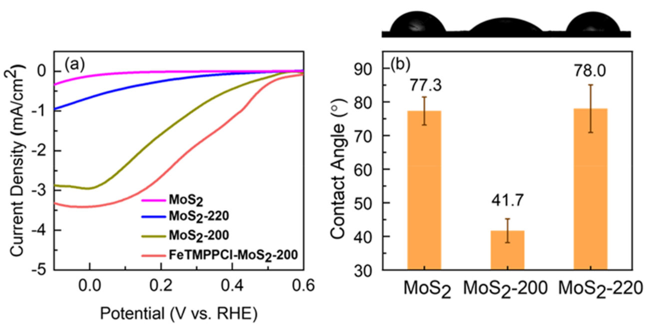


**Figure 7.** (a) Ar-subtracted LSV of $MoS_2$, $MoS_2$-220, $MoS_2$-200, and FeTMPPCl-$MoS_2$-200 obtained in 0.1 M $HClO_4$ at a rotation rate of 1600 rpm. (b) The average contact angle values for water measured on $MoS_2$, $MoS_2$-200, and $MoS_2$-220 pellets.

$O_2$-saturated 0.1 M $HClO_4$. Voltammetry from $MoS_2$-200 or FeTMPPCl-$MoS_2$-200 in Ar-saturated solution was highly capacitive as expected due to the larger $c$-axis spacing in $MoS_2$-200.[39] ICP results did not detect the presence of Fe in solution following immersion of FeTMPPCl-$MoS_2$-200 into electrolyte (Table S1). Figure 7a shows that $MoS_2$-200 exhibits an ORR onset substantially more positive (ca. 400 mV) relative to either $MoS_2$ or $MoS_2$-220. Additionally, FeTMPPCl-$MoS_2$-200 exhibits an ORR $E_{1/2}$ some 50 mV more positive than $MoS_2$-200. Thus, processing the $MoS_2$ to incorporate more O leads to enhanced ORR activity relative to $MoS_2$ alone.

To evaluate the origin of the enhanced activity of $MoS_2$-200, we performed contact angle measurements for both $MoS_2$-200



https://doi.org/10.1021/acscatal.1c04871
ACS Catal. 2022, 12, 1139−1149

and $MoS_2$-220. Figure 7b reports that $MoS_2$-200 exhibits a contact angle of 41.7°, while the contact angle obtained for both $MoS_2$ and $MoS_2$-220 is around 78°. The decreased contact angle for $MoS_2$-200 suggests this O-incorporated material is more hydrophilic than $MoS_2$-220 or $MoS_2$. We note that the contact angle for $MoS_2$-200 is consistent with that reported for XC72. Taken together, these results suggest that water availability is important for ORR activity in these materials.

## ■ DISCUSSION

The results reported above show that FeTMPPCl adsorbed on different supports exhibits widely different ORR activities depending on the support. Figure 8 reprises the ORR data.

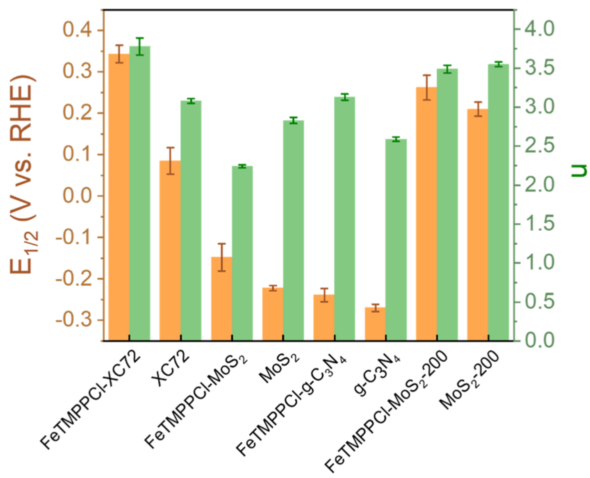


**Figure 8.** Comparison of $E_{1/2}$ and $n$ values for FeTMPPCl adsorbed on different supports, along with values from the supports alone.

Figure 8 shows that changing the support leads to dramatic changes in ORR activity. FeTMPPCl adsorbed on XC72 is most active, while FeTMPPCl on $g\text{-}C_3N_4$ has an $E_{1/2}$ some 500 mV more negative. Additionally, the results above show that adding porphyrin to the support yields dramatically increased ORR activity on XC72 but only a small change in ORR activity on $MoS_2$ or $g\text{-}C_3N_4$. Nearly 4 electrons are transferred when FeTMPPCl is on XC72 support, but that number is nearer to 3 for the other supports.

Detailed characterization reported above shows that the changes in activity seen in Figure 8 do not relate to changes in the coordination environment around the Fe center when FeTMPPCl is adsorbed on the different supports. The nearly identical EPR, EXAFS, and magnetometry for each sample show that the act of adsorbing FeTMPPCl on different supports does not change the electronic structure around the Fe center. At the same time, ICP shows that FeTMPPCl is well adsorbed on each support and that there is no dissolution of Fe before or during ORR activity. The linear field response in the magnetometry further indicates that there is no superparamagnetic or ferromagnetic material in the samples. EXAFS further suggests the presence of only a weak interaction between the Fe center and the support.

While there is no apparent difference in the coordination environment around the Fe center in all the supports considered here, there is a difference in the pH dependence of the ORR $E_{1/2}$ for the three materials. In particular, FeTMPPCl-XC72 exhibits a strong pH dependence, but this pH dependence is not found with the other two supports. Interestingly, results from FeTMPPCl-XC72 show that $E_{1/2}$ decreases going to pH = 3 before increasing again going to pH = 6. This behavior was seen in one prior paper (albeit using pyrolyzed materials)[71] and attributed to interaction of functional groups on the XC72 with the electrolyte. The $pK_a$ of carboxylic acid on the electrode is ca. 4.5, and deprotonation of these groups may allow for more proton availability at the electrode surface at higher pH values. Our data (Figure 6) show that bare XC72 exhibits a trend in an ORR onset similar to that seen with FeTMPPCl-XC72 in that the onset is high at pH = 1, decreases to pH = 3, and then increases to pH = 6. Neither $MoS_2$ nor $g\text{-}C_3N_4$ exhibits substantial pH dependence in an ORR onset with or without the presence of FeTMPPCl.

The presence of a pH dependence for ORR on XC72 suggests that the approach of water and protons is crucial to ORR activity in the supported catalyst. Indeed, the nonunity kinetic isotope effect (KIE) seen from pyrolyzed Fe-containing materials on XC72 suggests a strong proton dependence in the rate-determining step (RDS) for Fe ORR catalysts supported on the electrode.[76] While we did not measure the KIE for the catalysts considered in this paper, the KIE in wild-type cytochrome *c* oxidase (a heme-based ORR enzyme) is ca. 2 for the $P^3 \rightarrow F^3$ transition and ca. 7 for the $F^3 \rightarrow O^4$ transition.[77−79] These nonunity KIE values strongly support the participation of proton during or before the RDS. If proton availability is lower in the $MoS_2$ and $g\text{-}C_3N_4$ materials, this lowered availability has been shown to inhibit the ORR, leading to more pronounced peroxide formation.[80]

The origin of the increased participation of protons for XC72 must be related to the increased hydrophilicity of this material relative to $MoS_2$ or $g\text{-}C_3N_4$. A more hydrophobic surface will inhibit the approach of protons and diminishes the potential dependence of the water structure above such a surface.[81] The relationship between hydrophilicity or hydrophobicity and the ORR has a long history. For example, a review article[82] suggests that ORR is enhanced by multiphase mass transfer diffusion of reactants ($O_2$, $H^+/e^-$) and products between the electrochemical surface and the electrolyte. Surface reactions, including oxygen adsorption, interfacial charge transfer, and desorption of intermediates/products near the active sites, are increased in more hydrophilic materials. This insight is supported by studies on oxidized carbons,[83] O-doped carbon-supported single-Fe-site catalysts,[84] N-doped porous carbon materials,[85] superhydrophilic $O_2$-entrapping honeycomb carbon nanofibers,[86] and edge-selectively functionalized graphene nanoplatelets.[87] A few studies suggest that more hydrophobic surfaces or surfaces with intermediate hydrophobicity are more active for the ORR. In these cases, hydrophobicity is induced through the adsorption of various ionic liquids[88,89] or occurs on zerovalent metal electrodes,[90] where the ORR mechanism may be different from that considered here.[76] The increased hydrophilicity may also promote stronger interaction of Nafion with the support.

Above we show that we can activate $MoS_2$ to make it more hydrophilic relative to unactivated $MoS_2$. Consistent with the above suggestions, FeTMPPCl supported on the activated $MoS_2$ exhibits a substantially more positive $E_{1/2}$ for the ORR relative to the unactivated $MoS_2$ and also exhibits a higher n value. While the *c*-axis spacing in $MoS_2$-200 is larger than that in the unactivated samples, the real origin of the enhanced activity is the greater affinity for water (lower contact angle)



https://doi.org/10.1021/acscatal.1c04871
ACS Catal. 2022, 12, 1139−1149

that $MoS_2$-200 exhibits relative to the other samples. This observation again suggests that the interaction of the support with the electrolyte controls much of the ORR activity.

## CONCLUSIONS

This study shows that the interaction of the catalysts and the support with the electrolyte is important in determining ORR activity. While the coordination environment around the Fe remains the same in all three supports, the interaction of the support-porphyrin complex with the solvent is very different. XC72 wets better than the other substrates and exhibits higher activity. If the approach of water to the support is inhibited, then the ORR activity is inhibited, and peroxide production increases due to insufficient proton activity at the active site. If proton activity is increased, then four electron reduction of oxygen to water is enhanced.

## ASSOCIATED CONTENT

### Supporting Information

The Supporting Information is available free of charge at https://pubs.acs.org/doi/10.1021/acscatal.1c04871.

Koutecký-Levich plot, additional voltammetry, Fe% determined by ICP-OES, XPS data, and fitting data and parameters for EPR, EXAFS, and XPS (PDF)

## AUTHOR INFORMATION


### Corresponding Author

**Andrew A. Gewirth** − *Department of Chemistry, University of Illinois at Urbana−Champaign, Urbana, Illinois 61801, United States*; orcid.org/0000-0003-4400-9907; Phone: 217-333-8329; Email: agewirth@illinois.edu; Fax: 217-244-3186

### Authors

**Qi Hua** − *Department of Chemistry, University of Illinois at Urbana−Champaign, Urbana, Illinois 61801, United States*; orcid.org/0000-0002-7857-6638

**Kenneth E. Madsen** − *Department of Chemistry, University of Illinois at Urbana−Champaign, Urbana, Illinois 61801, United States*

**Anne Marie Esposito** − *Department of Chemistry, University of Illinois at Urbana−Champaign, Urbana, Illinois 61801, United States*

**Xinyi Chen** − *Department of Chemistry, University of Illinois at Urbana−Champaign, Urbana, Illinois 61801, United States*; orcid.org/0000-0002-6990-5233

**Toby J. Woods** − *Department of Chemistry, University of Illinois at Urbana−Champaign, Urbana, Illinois 61801, United States*; orcid.org/0000-0002-1737-811X

**Richard T. Haasch** − *Frederick Seitz Materials Research Laboratory, University of Illinois at Urbana−Champaign, Urbana, Illinois 61801, United States*; orcid.org/0000-0001-9479-2595

**Shuting Xiang** − *Department of Materials Science and Chemical Engineering, Stony Brook University, Stony Brook, New York 11794, United States*

**Anatoly I. Frenkel** − *Department of Materials Science and Chemical Engineering, Stony Brook University, Stony Brook, New York 11794, United States; Division of Chemistry, Brookhaven National Laboratory, Upton, New York 11973, United States*; orcid.org/0000-0002-5451-1207

**Timothy T. Fister** − *Chemical Sciences and Engineering Division, Argonne National Laboratory, Argonne, Illinois 60439, United States*; orcid.org/0000-0001-6537-6170

Complete contact information is available at: https://pubs.acs.org/10.1021/acscatal.1c04871


### Notes

The authors declare no competing financial interest.

## ACKNOWLEDGMENTS

Q.H. acknowledges a Chia-Chen Chu fellowship. The National Science Foundation (2029326) is gratefully acknowledged for support of this research. Major funding for the Bruker EMXPlus was provided by a National Science Foundation Award 1726244 (2017) to the School of Chemical Sciences EPR Lab. XAS analysis by A.I.F. was supported by the National Science Foundation under Grant No. CHE-2102299. XPS and SQUID magnetometry was carried out in part in the Materials Research Laboratory Central Research Facilities, University of Illinois.

## REFERENCES


(1) Chen, Z.; Higgins, D.; Yu, A.; Zhang, L.; Zhang, J. A Review on Non-Precious Metal Electrocatalysts for PEM Fuel Cells. *Energy Environ. Sci.* **2011**, *4* (9), 3167−3192.

(2) Ma, R.; Lin, G.; Zhou, Y.; Liu, Q.; Zhang, T.; Shan, G.; Yang, M.; Wang, J. A Review of Oxygen Reduction Mechanisms for Metal-Free Carbon-Based Electrocatalysts. *Npj Comput. Mater.* **2019**, *5*, 78.

(3) Gewirth, A. A.; Varnell, J. A.; DiAscro, A. M. Nonprecious Metal Catalysts for Oxygen Reduction in Heterogeneous Aqueous Systems. *Chem. Rev.* **2018**, *118* (5), 2313−2339.

(4) Jiao, Y.; Zheng, Y.; Jaroniec, M.; Qiao, S. Z. Design of Electrocatalysts for Oxygen- and Hydrogen-Involving Energy Conversion Reactions. *Chem. Soc. Rev.* **2015**, *44* (8), 2060−2086.

(5) Gewirth, A. A.; Thorum, M. S. Electroreduction of Dioxygen for Fuel-Cell Applications: Materials and Challenges. *Inorg. Chem.* **2010**, *49* (8), 3557−3566.

(6) Gorlin, Y.; Jaramillo, T. F. A Bifunctional Nonprecious Metal Catalyst for Oxygen Reduction and Water Oxidation. *J. Am. Chem. Soc.* **2010**, *132* (39), 13612−13614.

(7) Wu, G.; Zelenay, P. Nanostructured Nonprecious Metal Catalysts for Oxygen Reduction Reaction. *Acc. Chem. Res.* **2013**, *46* (8), 1878−1889.

(8) Zhu, C.; Li, H.; Fu, S.; Du, D.; Lin, Y. Highly Efficient Nonprecious Metal Catalysts Towards Oxygen Reduction Reaction Based on Three-Dimensional Porous Carbon Nanostructures. *Chem. Soc. Rev.* **2016**, *45* (3), 517−531.

(9) Cao, R.; Thapa, R.; Kim, H.; Xu, X.; Gyu Kim, M.; Li, Q.; Park, N.; Liu, M.; Cho, J. Promotion of Oxygen Reduction by a Bio-Inspired Tethered Iron Phthalocyanine Carbon Nanotube-Based Catalyst. *Nat. Commun.* **2013**, *4*, 2076.

(10) Jasinski, R. Cobalt Phthalocyanine as a Full Cell Cathode. *J. Electrochem. Soc.* **1965**, *112* (5), 526−528.

(11) Zitolo, A.; Goellner, V.; Armel, V.; Sougrati, M.-T.; Mineva, T.; Stievano, L.; Fonda, E.; Jaouen, F. Identification of Catalytic Sites for Oxygen Reduction in Iron- and Nitrogen-Doped Graphene Materials. *Nat. Mater.* **2015**, *14* (9), 937−944.

(12) Dominguez, C.; Perez-Alonso, F. J.; Salam, M. A.; Al-Thabaiti, S. A.; Pena, M. A.; Barrio, L.; Rojas, S. Effect of the N Content of Fe/N/Graphene Catalysts for the Oxygen Reduction Reaction in Alkaline Media. *J. Mater. Chem. A* **2015**, *3* (48), 24487−24494.

(13) Zhu, J.; Xiao, M.; Liu, C.; Ge, J.; St-Pierre, J.; Xing, W. Growth Mechanism and Active Site Probing of $Fe_3C$@N-Doped Carbon Nanotubes/C Catalysts: Guidance for Building Highly Efficient Oxygen Reduction Electrocatalysts. *J. Mater. Chem. A* **2015**, *3* (43), 21451−21459.

(14) Varnell, J. A.; Tse, E. C. M.; Schulz, C. E.; Fister, T. T.; Haasch, R. T.; Timoshenko, J.; Frenkel, A. I.; Gewirth, A. A. Identification of Carbon-Encapsulated Iron Nanoparticles as Active Species in Non-Precious Metal Oxygen Reduction Catalysts. *Nat. Commun.* **2016**, *7*, 12582.
(15) Wu, G.; More, K. L.; Johnston, C. M.; Zelenay, P. High-Performance Electrocatalysts for Oxygen Reduction Derived from Polyaniline, Iron, and Cobalt. *Science* **2011**, *332* (6028), 443−447.
(16) Zhao, Y.-M.; Yu, G.-Q.; Wang, F.-F.; Wei, P.-J.; Liu, J.-G. Bioinspired Transition-Metal Complexes as Electrocatalysts for the Oxygen Reduction Reaction. *Chem.—Eur. J.* **2019**, *25* (15), 3726−3739.
(17) Jasinski, R. A New Fuel Cell Cathode Catalyst. *Nature* **1964**, *201*, 1212−1213.
(18) Zion, N.; Friedman, A.; Levy, N.; Elbaz, L. Bioinspired Electrocatalysis of Oxygen Reduction Reaction in Fuel Cells Using Molecular Catalysts. *Adv. Mater.* **2018**, *30* (41), 1800406.
(19) Riquelme, J.; Neira, K.; Marco, J. F.; Hermosilla-Ibáñez, P.; Orellana, W.; Zagal, J. H.; Tasca, F. Biomimicking Vitamin B12. A Co Phthalocyanine Pyridine Axial Ligand Coordinated Catalyst for the Oxygen Reduction Reaction. *Electrochim. Acta* **2018**, *265*, 547−555.
(20) Hijazi, I.; Bourgeteau, T.; Cornut, R.; Morozan, A.; Filoramo, A.; Leroy, J.; Derycke, V.; Jousselme, B.; Campidelli, S. Carbon Nanotube-Templated Synthesis of Covalent Porphyrin Network for Oxygen Reduction Reaction. *J. Am. Chem. Soc.* **2014**, *136* (17), 6348−6354.
(21) Tang, H.; Yin, H.; Wang, J.; Yang, N.; Wang, D.; Tang, Z. Molecular Architecture of Cobalt Porphyrin Multilayers on Reduced Graphene Oxide Sheets for High-Performance Oxygen Reduction Reaction. *Angew. Chem., Int. Ed.* **2013**, *52*, 5585−5589.
(22) Jahan, M.; Bao, Q.; Loh, K. P. Electrocatalytically Active Graphene−Porphyrin MOF Composite for Oxygen Reduction Reaction. *J. Am. Chem. Soc.* **2012**, *134* (15), 6707−6713.
(23) Zuo, Q.; Cheng, G.; Luo, W. A Reduced Graphene Oxide/ Covalent Cobalt Porphyrin Framework for Efficient Oxygen Reduction Reaction. *Dalton Trans.* **2017**, *46* (29), 9344−9348.
(24) Chattopadhyay, S.; Sarkar, A.; Chatterjee, S.; Dey, A. Functional Adlayers on Au Electrodes: Some Recent Applications in Hydrogen Evolution and Oxygen Reduction. *J. Mater. Chem. A* **2018**, *6* (4), 1323−1339.
(25) Collman, J. P.; Devaraj, N. K.; Decreau, R. A.; Yang, Y.; Yan, Y.-L.; Ebina, W.; Eberspacher, T. A.; Chidsey, C. E. D. A Cytochrome C Oxidase Model Catalyzes Oxygen to Water Reduction under Rate-Limiting Electron Flux. *Science* **2007**, *315* (5818), 1565−1568.
(26) Facchin, A.; Kosmala, T.; Gennaro, A.; Durante, C. Electrochemical Scanning Tunneling Microscopy Investigations of $FeN_4$-Based Macrocyclic Molecules Adsorbed on Au(111) and Their Implications in the Oxygen Reduction Reaction. *ChemElectroChem.* **2020**, *7* (6), 1431−1437.
(27) Herrera, S.; Tasca, F.; Williams, F. J.; Calvo, E. J. Adsorption of 4,4-Dithiodipyridine Axially Coordinated to Iron(II) Phthalocyanine on Au(111) as a New Strategy for Oxygen Reduction Electrocatalysis. *ChemPhysChem* **2018**, *19* (13), 1599−1604.
(28) Hosseini, A.; Barile, C. J.; Devadoss, A.; Eberspacher, T. A.; Decreau, R. A.; Collman, J. P. Hybrid Bilayer Membrane: A Platform to Study the Role of Proton Flux on the Efficiency of Oxygen Reduction by a Molecular Electrocatalyst. *J. Am. Chem. Soc.* **2011**, *133* (29), 11100−11102.
(29) Olguin, C. F.; Agurto, N.; Silva, C. P.; Candia, C. P.; Santander-Nelli, M.; Oyarzo, J.; Gomez, A.; Silva, J. F.; Pavez, J. Tuning the Covering on Gold Surfaces by Grafting Amino-Aryl Films Functionalized with Fe(II) Phthalocyanine: Performance on the Electrocatalysis of Oxygen Reduction. *Molecules* **2021**, *26* (6), 1631.
(30) Pizarro, A.; Abarca, G.; Gutierrez-Ceron, C.; Cortes-Arriagada, D.; Bernardi, F.; Berrios, C.; Silva, J. F.; Rezende, M. C.; Zagal, J. H.; Onate, R.; Ponce, I. Building Pyridinium Molecular Wires as Axial Ligands for Tuning the Electrocatalytic Activity of Iron Phthalocyanines for the Oxygen Reduction Reaction. *ACS Catal.* **2018**, *8* (9), 8406−8419.
(31) Samanta, S.; Sengupta, K.; Mittra, K.; Bandyopadhyay, S.; Dey, A. Selective Four Electron Reduction of $O_2$ by an Iron Porphyrin Electrocatalyst under Fast and Slow Electron Fluxes. *Chem. Commun.* **2012**, *48* (61), 7631−7633.
(32) Zhou, Y.; Xing, Y.; Wen, J.; Ma, H.; Wang, F.; Xia, X. Axial Ligands Tailoring the ORR Activity of Cobalt Porphyrin. *Sci. Bull.* **2019**, *64* (16), 1158−1166.
(33) Kwon, I. S.; Kwak, I. H.; Kim, J. Y.; Abbas, H. G.; Debela, T. T.; Seo, J.; Cho, M. K.; Ahn, J.-P.; Park, J.; Kang, H. S. Two-Dimensional $MoS_2$/Fe-Phthalocyanine Hybrid Nanostructures as Excellent Electrocatalysts for Hydrogen Evolution and Oxygen Reduction Reactions. *Nanoscale* **2019**, *11* (30), 14266−14275.
(34) Singh, D. K.; Ganesan, V.; Yadav, D. K.; Yadav, M. Metal (Mn, Fe, Co, Ni, Cu, and Zn) Phthalocyanine-Immobilized Mesoporous Carbon Nitride Materials as Durable Electrode Modifiers for the Oxygen Reduction Reaction. *Langmuir* **2020**, *36* (41), 12202−12212.
(35) Singh, D. K.; Ganesan, V.; Yadav, D. K.; Yadav, M.; Sonkar, P. K.; Gupta, R. Mesoporous Carbon Nitride Supported 5,10,15,20-Tetrakis(4-Methoxyphenyl)-21H,23H-Porphine Cobalt(II) as a Selective and Durable Electrocatalyst for the Production of Hydrogen Peroxide Via Two-Electron Oxygen Reduction. *Catal. Sci. Technol.* **2021**, *11* (3), 1014−1026.
(36) Médard, C.; Lefèvre, M.; Dodelet, J. P.; Jaouen, F.; Lindbergh, G. Oxygen Reduction by Fe-Based Catalysts in PEM Fuel Cell Conditions: Activity and Selectivity of the Catalysts Obtained with Two Fe Precursors and Various Carbon Supports. *Electrochim. Acta* **2006**, *51* (16), 3202−3213.
(37) Dong, F.; Wang, Z.; Sun, Y.; Ho, W.-K.; Zhang, H. Engineering the Nanoarchitecture and Texture of Polymeric Carbon Nitride Semiconductor for Enhanced Visible Light Photocatalytic Activity. *J. Colloid Interface Sci.* **2013**, *401*, 70−79.
(38) Zhang, W.; Zhou, L.; Deng, H. P. Ag Modified g-$C_3N_4$ Composites with Enhanced Visible-Light Photocatalytic Activity for Diclofenac Degradation. *J. Mol. Catal. A: Chem.* **2016**, *423*, 270−276.
(39) Xie, J.; Zhang, J.; Li, S.; Grote, F.; Zhang, X.; Zhang, H.; Wang, R.; Lei, Y.; Pan, B.; Xie, Y. Controllable Disorder Engineering in Oxygen-Incorporated $MoS_2$ Ultrathin Nanosheets for Efficient Hydrogen Evolution. *J. Am. Chem. Soc.* **2013**, *135*, 17881−17888.
(40) Xie, J.; Zhang, H.; Li, S.; Wang, R.; Sun, X.; Zhou, M.; Zhou, J.; Lou, X. W.; Xie, Y. Defect-Rich $MoS_2$ Ultrathin Nanosheets with Additional Active Edge Sites for Enhanced Electrocatalytic Hydrogen Evolution. *Adv. Mater.* **2013**, *25*, 5807−5813.
(41) Zhang, X. H.; Wang, C.; Xue, M. Q.; Lin, B. C.; Ye, X.; Lei, W. N. Hydrothermal Synthesis and Characterization of Ultrathin $MoS_2$ Nanosheets. *Chalcogenide Lett.* **2016**, *13* (1), 27−34.
(42) Britton, H. T. S.; Robinson, R. A. Cxcviii.—Universal Buffer Solutions and the Dissociation Constant of Veronal. *Journal of the Chemical Society (Resumed)* **1931**, *0*, 1456−1462.
(43) Stoll, S.; Schweiger, A. Easyspin, a Comprehensive Software Package for Spectral Simulation and Analysis in EPR. *J. Magn. Reson.* **2006**, *178* (1), 42−55.
(44) Ravel, B.; Newville, M. Athena, Artemis, Hephaestus: Data Analysis for X-Ray Absorption Spectroscopy Using IFEFFIT. *J. Synchrotron Radiat.* **2005**, *12*, 537−541.
(45) Zabinsky, S. I.; Rehr, J. J.; Ankudinov, A.; Albers, R. C.; Eller, M. J. Multiple-Scattering Calculations of X-Ray-Absorption Spectra. *Phys. Rev. B* **1995**, *52* (4), 2995−3009.
(46) Zhong, X.; Liu, L.; Wang, X.; Yu, H.; Zhuang, G.; Mei, D.; Li, X.; Wang, J. G. A Radar-Like Iron Based Nanohybrid as an Efficient and Stable Electrocatalyst for Oxygen Reduction. *J. Mater. Chem. A* **2014**, *2*, 6703−6707.
(47) Birry, L.; Zagal, J. H.; Dodelet, J. P. Does Co Poison Fe-Based Catalysts for ORR? *Electrochem. Commun.* **2010**, *12*, 628−631.
(48) Wang, X.; Zheng, T.; Tang, Y.; Li, X.; Rykov, A. I.; Li, X.; Wang, J.; He, Q.; Cheng, J.; Zhang, X. The Effect of Tuning the Coordination Sphere of Iron Complexes for the Oxygen Reduction Reaction in Acidic Media. *J. Electrochem. Soc.* **2021**, *168*, 044506.
(49) Rowley-Neale, S. J.; Fearn, J. M.; Brownson, D. A.; Smith, G. C.; Ji, X.; Banks, C. E. 2D Molybdenum Disulphide (2D-$MoS_2$)

Modified Electrodes Explored Towards the Oxygen Reduction Reaction. *Nanoscale* **2016**, *8* (31), 14767−14777.

(50) He, T.; Xu, L.; Zhang, Y.; Huang, H.; Jiao, H. High-Quality Vanadium-Doped $MoS_2$ Ultrathin Nanosheets as an Efficient ORR Catalyst. *New J. Chem.* **2019**, *43* (3), 1611−1616.

(51) Wang, M.; Wu, Z.; Dai, L. Graphitic Carbon Nitrides Supported by Nitrogen-Doped Graphene as Efficient Metal-Free Electrocatalysts for Oxygen Reduction. *J. Electroanal. Chem.* **2015**, *753*, 16−20.

(52) Pérez-Rodríguez, S.; Pastor, E.; Lázaro, M. J. Electrochemical Behavior of the Carbon Black Vulcan XC-72R: Influence of the Surface Chemistry. *Int. J. Hydrogen Energy* **2018**, *43* (16), 7911−7922.

(53) Geng, X.; Sun, W.; Wu, W.; Chen, B.; Al-Hilo, A.; Benamara, M.; Zhu, H.; Watanabe, F.; Cui, J.; Chen, T.-p. Pure and Stable Metallic Phase Molybdenum Disulfide Nanosheets for Hydrogen Evolution Reaction. *Nat. Commun.* **2016**, *7* (1), 10672.

(54) Zhang, Y.; Mori, T.; Ye, J.; Antonietti, M. Phosphorus-Doped Carbon Nitride Solid: Enhanced Electrical Conductivity and Photocurrent Generation. *J. Am. Chem. Soc.* **2010**, *132* (18), 6294−6295.

(55) Velický, M.; Bissett, M. A.; Toth, P. S.; Patten, H. V.; Worrall, S. D.; Rodgers, A. N. J.; Hill, E. W.; Kinloch, I. A.; Novoselov, K. S.; Georgiou, T.; Britnell, L.; Dryfe, R. A. W. Electron Transfer Kinetics on Natural Crystals of $MoS_2$ and Graphite. *Phys. Chem. Chem. Phys.* **2015**, *17* (27), 17844−17853.

(56) Wagner, S.; Auerbach, H.; Tait, C. E.; Martinaiou, I.; Kumar, S. C.; Kübel, C.; Sergeev, I.; Wille, H. C.; Behrends, J.; Wolny, J. Elucidating the Structural Composition of an Fe−N−C Catalyst by Nuclear-and Electron-Resonance Techniques. *Angew. Chem., Int. Ed.* **2019**, *58* (31), 10486−10492.

(57) Boulic, F.; Brosseau, C.; Le Mest, Y.; Loaëc, J.; Carmona, F. Absorbency Properties and Electron Paramagnetic Resonance Characterization of Polymeric Carbon Black Composites. *J. Phys. D: Appl. Phys.* **1998**, *31*, 1904−1912.

(58) Saab, E.; Abi-Aad, E.; Bokova, M. N.; Zhilinskaya, E. A.; Aboukaïs, A. EPR Characterisation of Carbon Black in Loose and Tight Contact with $Al_2O_3$ and $CeO_2$ Catalysts. *Carbon* **2007**, *45*, 561−567.

(59) González, J. R.; Alcántara, R.; Tirado, J. L.; Fielding, A. J.; Dryfe, R. A. W. Electrochemical Interaction of Few-Layer Molybdenum Disulfide Composites Vs Sodium: New Insights on the Reaction Mechanism. *Chem. Mater.* **2017**, *29*, 5886−5895.

(60) Singh, M. K.; Chettri, P.; Tripathi, A.; Tiwari, A.; Mukherjee, B.; Mandal, R. K. Defect Mediated Magnetic Transitions in Fe and Mn Doped $MoS_2$. *Phys. Chem. Chem. Phys.* **2018**, *20*, 15817−15823.

(61) Fang, J.; Fan, H.; Li, M.; Long, C. Nitrogen Self-Doped Graphitic Carbon Nitride as Efficient Visible Light Photocatalyst for Hydrogen Evolution. *J. Mater. Chem. A* **2015**, *3*, 13819−13826.

(62) Wang, J.; Yang, Z.; Yao, W.; Gao, X.; Tao, D. Defects Modified in the Exfoliation of g-$C_3N_4$ Nanosheets Via a Self-Assembly Process for Improved Hydrogen Evolution Performance. *Appl. Catal., B* **2018**, *238*, 629−637.

(63) Russell, S. *Physical Methods for Chemists*, 2nd ed.; Surfside Scientific: Gainesville, FL, 1977; p 476.

(64) Kramm, U. I.; Herrmann-Geppert, I.; Behrends, J.; Lips, K.; Fiechter, S.; Bogdanoff, P. On an Easy Way to Prepare Metal−Nitrogen Doped Carbon with Exclusive Presence of $MeN_4$-Type Sites Active for the ORR. *J. Am. Chem. Soc.* **2016**, *138* (2), 635−640.

(65) Huang, H.; Wang, C.; Shown, I.; Chang, S.; Hsu, H.; Du, H.; Chen, L.; Chen, K. High-Performance Pyrolyzed Iron Corrole as a Potential Non-Precious Metal Catalyst for PEMFCS. *J. Mater. Chem. A* **2013**, *1* (46), 14692−14699.

(66) Cheon, J. Y.; Kim, T.; Choi, Y.; Jeong, H. Y.; Kim, M. G.; Sa, Y. J.; Kim, J.; Lee, Z.; Yang, T.; Kwon, K.; Terasaki, O.; Park, G.; Adzic, R. R.; Joo, S. H. Ordered Mesoporous Porphyrinic Carbons with Very High Electrocatalytic Activity for the Oxygen Reduction Reaction. *Sci. Rep.* **2013**, *3* (1), 2715.

(67) Li, J.; Ghoshal, S.; Liang, W.; Sougrati, M. T.; Jaouen, F.; Halevi, B.; McKinney, S.; McCool, G.; Ma, C.; Yuan, X.; Ma, Z.; Mukerjee, S.; Jia, Q. Structural and Mechanistic Basis for the High Activity of Fe−N−C Catalysts toward Oxygen Reduction. *Energy Environ. Sci.* **2016**, *9* (7), 2418−2432.

(68) Roy, M.; Gurman, S. J.; vanDorssen, G. The Amplitude Reduction Factor in EXAFS. *J. Phys. IV* **1997**, *7* (C2), 151−152.

(69) Ravel, B.; Kelly, S. D. The Difficult Chore of Measuring Coordination by EXAFS. *AIP Conf Proc.* **2006**, *882*, 150−152.

(70) Gericke, R.; Doyle, L. M.; Farquhar, E. R.; McDonald, A. R. Oxo-Free Hydrocarbon Oxidation by an Iron(III)-Isoporphyrin Complex. *Inorg. Chem.* **2020**, *59* (19), 13952−13961.

(71) Rojas-Carbonell, S.; Artyushkova, K.; Serov, A.; Santoro, C.; Matanovic, I.; Atanassov, P. Effect of pH on the Activity of Platinum Group Metal-Free Catalysts in Oxygen Reduction Reaction. *ACS Catal.* **2018**, *8* (4), 3041−3053.

(72) Paz, E. C.; Aveiro, L. R.; Pinheiro, V. S.; Souza, F. M.; Lima, V. B.; Silva, F. L.; Hammer, P.; Lanza, M. R. V.; Santos, M. C. Evaluation of $H_2O_2$ Electrogeneration and Decolorization of Orange II Azo Dye Using Tungsten Oxide Nanoparticle-Modified Carbon. *Appl. Catal., B* **2018**, *232*, 436−445.

(73) Gurarslan, A.; Jiao, S.; Li, T. D.; Li, G.; Yu, Y.; Gao, Y.; Riedo, E.; Xu, Z.; Cao, L. Van Der Waals Force Isolation of Monolayer $MoS_2$. *Adv. Mater.* **2016**, *28*, 10055−10060.

(74) Mao, Z.; Chen, J.; Yang, Y.; Bie, L.; Fahlman, B. D.; Wang, D. Modification of Surface Properties and Enhancement of Photocatalytic Performance for g-$C_3N_4$ Via Plasma Treatment. *Carbon* **2017**, *123*, 651−659.

(75) Zheng, Z.; Cong, S.; Gong, W.; Xuan, J.; Li, G.; Lu, W.; Geng, F.; Zhao, Z. Semiconductor SERS Enhancement Enabled by Oxygen Incorporation. *Nat. Commun.* **2017**, *8* (1), 1993.

(76) Tse, E. C. M.; Varnell, J. A.; Hoang, T. T. H.; Gewirth, A. A. Elucidating Proton Involvement in the Rate-Determining Step for Pt/Pd-Based and Non-Precious-Metal Oxygen Reduction Reaction Catalysts Using the Kinetic Isotope Effect. *J. Phys. Chem. Lett.* **2016**, *7* (18), 3542−3547.

(77) Salomonsson, L.; Brändén, G.; Brzezinski, P. Deuterium Isotope Effect of Proton Pumping in Cytochrome C Oxidase. *Biochim Biophys Acta Bioenerg* **2008**, *1777* (4), 343−350.

(78) Ådelroth, P.; Karpefors, M.; Gilderson, G.; Tomson, F. L.; Gennis, R. B.; Brzezinski, P. Proton Transfer from Glutamate 286 Determines the Transition Rates between Oxygen Intermediates in Cytochrome C Oxidase. *Biochim Biophys Acta Bioenerg* **2000**, *1459* (2), 533−539.

(79) Johansson, A.-L.; Chakrabarty, S.; Berthold, C. L.; Högbom, M.; Warshel, A.; Brzezinski, P. Proton-Transport Mechanisms in Cytochrome C Oxidase Revealed by Studies of Kinetic Isotope Effects. *Biochim Biophys Acta Bioenerg* **2011**, *1807* (9), 1083−1094.

(80) Tse, E. C. M.; Barile, C. J.; Kirchschlager, N. A.; Li, Y.; Gewargis, J. P.; Zimmerman, S. C.; Hosseini, A.; Gewirth, A. A. Proton Transfer Dynamics Control the Mechanism of $O_2$ Reduction by a Non-Precious Metal electrocatalyst. *Nat. Mater.* **2016**, *15* (7), 754−759.

(81) Shaw, S. K.; Gewirth, A. A. Potential Dependence of the Structure of Water at the Hydrophobic Liquid Interface. *J. Electroanal. Chem.* **2007**, *609* (2), 94−98.

(82) Qiao, M.; Titirici, M.-M. Engineering the Interface of Carbon Electrocatalysts at the Triple Point for Enhanced Oxygen Reduction Reaction. *Chem.—Eur. J.* **2018**, *24* (69), 18374−18384.

(83) Wang, X.; Ouyang, C.; Dou, S.; Liu, D.; Wang, S. Oxidized Carbon Nanotubes as an Efficient Metal-Free Electrocatalyst for the Oxygen Reduction Reaction. *RSC Adv.* **2015**, *5* (52), 41901−41904.

(84) Ni, W.; Gao, Y.; Zhang, Y.; Younus, H. A.; Guo, X.; Ma, C.; Zhang, Y.; Duan, J.; Zhang, J.; Zhang, S. O-Doping Boosts the Electrochemical Oxygen Reduction Activity of a Single Fe Site in Hydrophilic Carbon with Deep Mesopores. *ACS Appl. Mater. Interfaces* **2019**, *11* (49), 45825−45831.

(85) Huang, H.; Wei, X.; Gao, S. Nitrogen-Doped Porous Carbon Derived from Malachium Aquaticum Biomass as a Highly Efficient Electrocatalyst for Oxygen Reduction Reaction. *Electrochim. Acta* **2016**, *220*, 427−435.


https://doi.org/10.1021/acscatal.1c04871
*ACS Catal.* 2022, 12, 1139−1149

(86) Dong, K.; Liang, J.; Wang, Y.; Xu, Z.; Liu, Q.; Luo, Y.; Li, T.; Li, L.; Shi, X.; Asiri, A. M.; Li, Q.; Ma, D.; Sun, X. Honeycomb Carbon Nanofibers: A Superhydrophilic $O_2$-Entrapping Electrocatalyst Enables Ultrahigh Mass Activity for the Two-Electron Oxygen Reduction Reaction. *Angew. Chem.* **2021**, *133*, 10677−10681.
(87) Jeon, I.-Y.; Choi, H.-J.; Jung, S.-M.; Seo, J.-M.; Kim, M.-J.; Dai, L.; Baek, J.-B. Large-Scale Production of Edge-Selectively Functionalized Graphene Nanoplatelets Via Ball Milling and Their Use as Metal-Free Electrocatalysts for Oxygen Reduction Reaction. *J. Am. Chem. Soc.* **2013**, *135* (4), 1386−1393.
(88) Qiao, M.; Ferrero, G. A.; Fernández Velasco, L.; Vern Hor, W.; Yang, Y.; Luo, H.; Lodewyckx, P.; Fuertes, A. B.; Sevilla, M.; Titirici, M.-M. Boosting the Oxygen Reduction Electrocatalytic Performance of Nonprecious Metal Nanocarbons Via Triple Boundary Engineering Using Protic Ionic Liquids. *ACS Appl. Mater. Interfaces* **2019**, *11* (12), 11298−11305.
(89) Tang, C.; Wang, H.-F.; Zhang, Q. Multiscale Principles to Boost Reactivity in Gas-Involving Energy Electrocatalysis. *Acc. Chem. Res.* **2018**, *51* (4), 881−889.
(90) Wang, P.; Hayashi, T.; Meng, Q. a.; Wang, Q.; Liu, H.; Hashimoto, K.; Jiang, L. Highly Boosted Oxygen Reduction Reaction Activity by Tuning the Underwater Wetting State of the Superhydrophobic Electrode. *Small* **2017**, *13*, 1601250.





https://doi.org/10.1021/acscatal.1c04871
ACS Catal. 2022, 12, 1139−1149